Available online at www.sciencedirect.com
SCIENCE DIRECT
Journal of Power Sources 153 (2006) 76–88
JOURNAL OF POWER SOURCES
www.elsevier.com/locate/jpowsour

A quantitative study of the effect of flow-distributor geometry in the cathode of a PEM fuel cell

E. Birgersson [1], M. Vynnycky *

Department of Mechanics, FaxénLaboratoriet, KTH, SE-100 44, Stockholm, Sweden

Received 16 August 2004; received in revised form 8 March 2005; accepted 14 March 2005
Available online 14 June 2005

Abstract

An isothermal three-dimensional model describing mass, momentum and species transfer in the cathode of a proton exchange membrane fuel cell has been used to study four different flow-distributors: interdigitated, coflow and counterflow channels, and a foam. A quantitative comparison of the results shows that the interdigitated channels can sustain the highest current densities, followed in descending order by the foam, the counterflow and the coflow channels. The foam yields the most uniform current density distribution at higher currents, but care should be taken as to its permeability to avoid unreasonably high-pressure drops.

Keywords: Proton exchange membrane fuel cell; Flow fields; Current distribution

1. Introduction

In view of ever increasing levels of environmental pollution and thus a desire to replace the fossil-fuel-based economy with a cleaner alternative, the fuel cell has in recent years become a prime candidate as a power source for transport and stationary applications. The potential use of fuel cells ranges from distributed power sources and portable applications, such as laptops [1] or even for the future dismounted soldier [2], to vehicles.

One such type of cell is the proton exchange membrane fuel cell (PEMFC), a schematic representation of which is shown in Fig. 1. The basic cell consists of two porous electrodes, termed the anode and the cathode, separated by a proton conducting membrane. The porous electrodes are made of a composite material, containing carbon cloth and a hydrophobic agent, such as polytetrafluorethylene. Each electrode has a thin layer containing an electrocatalyst, such as platinum, that is dispersed on the carbon cloth and is in contact with the membrane, usually a hydrated perfluorinated sulfonic acid polymer. In addition a bipolar plate, essentially graphite into which flow and cooling channels have been machined, is situated adjacent to each electrode. In the course of operation, an oxidant, usually oxygen from air which is either dry or humidified to some extent, is fed at the inlet on the cathode side and transported to the electrolyte/cathode interface; the fuel on the other hand, normally hydrogen, is fed at the anode inlet and is transported to the electrolyte/anode interface. The reactions occurring at these interfaces are then

$$2H_2 \rightarrow 4H^+ + 4e^- \quad \text{at the anode}, \tag{1}$$

$$O_2 + 4H^+ \rightarrow 2H_2O \quad \text{at the cathode}, \tag{2}$$

which are termed the hydrogen oxidation reaction (HOR) and the oxygen reduction reaction (ORR), respectively. Thus, the protons produced at the anode are transported through the membrane to the cathode, whilst the electrons can drive a load through an external circuit.

In recent years, a number of mathematical models have been developed in an attempt to understand the phenomena

* Corresponding author. Tel.: +46 8 790 67 70; fax: +46 8 796 98 50.
E-mail address: michaelv@mech.kth.se (M. Vynnycky).
[1] Present address: Institute of High Performance Computing, 1 Science Park Road, #01-01 The Capricorn, Singapore Science Park II, Singapore 117528, Singapore.

0378-7753/$ – see front matter © 2005 Elsevier B.V. All rights reserved.
doi:10.1016/j.jpowsour.2005.03.211

Nomenclature

A	area (m^2)
$\mathcal{A}$	integration constant for asymptotic solution
$\mathcal{A}i_0$	volumetric exchange current density ($A\,m^{-3}$)
$\mathbf{B}$	transformation tensor
$\mathcal{B}$	integration constant for asymptotic solution
c	molar concentration ($mol\,m^{-3}$)
$\mathbf{D}$	diffusion tensor ($m^2\,s^{-1}$)
$\tilde{D}_{ij}$	diffusion coefficients for molar diffusive flux relative to a molar-averaged velocity ($m^2\,s^{-1}$)
$\overline{D}_{ij}$	diffusion coefficients for mass diffusive flux relative to a mass-averaged velocity ($m^2\,s^{-1}$)
$\mathcal{D}_{ij}$	binary Maxwell–Stefan diffusion coefficients ($m^2\,s^{-1}$)
$\mathfrak{D}$	effective oxygen permeability in the agglomerates ($mol\,m^{-1}\,s^{-1}$)
Δp	pressure drop ($N\,m^{-2}$)
$\mathbf{e}_x$, $\mathbf{e}_y$, $\mathbf{e}_z$	coordinate vectors
E	potential (V)
F	Faraday's constant ($As\,mol^{-1}$)
$\mathfrak{F}$	nucleus effectiveness factor for the agglomerate model
h	height (m)
$\mathfrak{H}$	relative humidity
i	current density ($A\,m^{-2}$)
$\langle i_v \rangle$	volume current density ($A\,m^{-3}$)
I	dimensionless current density
$\mathbf{K}$	permeability tensor (m^2)
L	length (m)
M	mean molecular mass ($kg\,mol^{-1}$)
$\mathcal{M}$	dimensionless mean molecular mass
M_i	molecular mass of species i ($kg\,mol^{-1}$)
$\mathcal{M}_i$	dimensionless molecular mass of species i
n	number of electrons consumed in the ORR per oxygen molecule
$\mathbf{n}$	unit vector in the normal direction
$\mathbf{n}_i$	mass flux of species i ($kg\,m^{-2}\,s^{-1}$)
p	pressure ($N\,m^{-2}$)
P	power density ($W\,m^{-2}$)
r	radius of agglomerate nucleus (m)
R	gas constant ($J\,mol^{-1}\,K^{-1}$)
Re	Reynolds number
S	denominator for transformation of diffusion coefficients ($m^2\,s^{-1}$)
$\mathbf{t}$	unit vector in the tangential direction
T	temperature (K)
$\boldsymbol{v}$	velocity ($m\,s^{-1}$)
$\mathcal{V}$	volume of the representative elementary volume (m^3)
w	width (m)
w_i	mass fraction of species i
$\mathbf{W}$	transformation tensor
x_i	molar fraction of species i
X,Y	dimensionless coordinates
$\mathbf{X}$	transformation tensor

Greek

α	coefficient for water transport by electro-osmosis in the membrane
α_r	cathodic transfer coefficient for the ORR
γ	porosity
δ_{ij}	Kronecker delta
$\Delta = 1/(Re\sigma^2)$	dimensionless parameter for asymptotic solution
ζ_i	dimensionless fraction of species i for asymptotic solution
η	overpotential (V)
κ	permeability (m^2)
μ	dynamic viscosity ($kg\,m^{-1}\,s^{-1}$)
ξ	stoichiometry
ρ	density ($kg\,m^{-3}$)
$\sigma = h_f/L$	dimensionless number
σ_{std}	standard deviation for current density ($A\,m^{-2}$)
Υ	parameter for current density expression
ϕ	general tensor
$\Phi = (2+4\alpha)\mathcal{M}_{H_2O} - \mathcal{M}_{O_2}$	dimensionless number
$\Omega = \Lambda/\sigma$	dimensionless number

Subscripts

0	equilibrium (reference)
a	active layer
cell	cell
p	porous backing
pol	polymer electrolyte in the active layer
f	flow channel
H_2O	water
O_2	oxygen
N_2	nitrogen
avg	average

Superscripts

cat	catalytic region
g	gas
in	inlet
out	outlet
ref	reference
vap	vaporization

Miscellaneous symbols

$\langle\rangle$	superficial average
$\langle\rangle^{(g)}$	intrinsic average
[]	scale

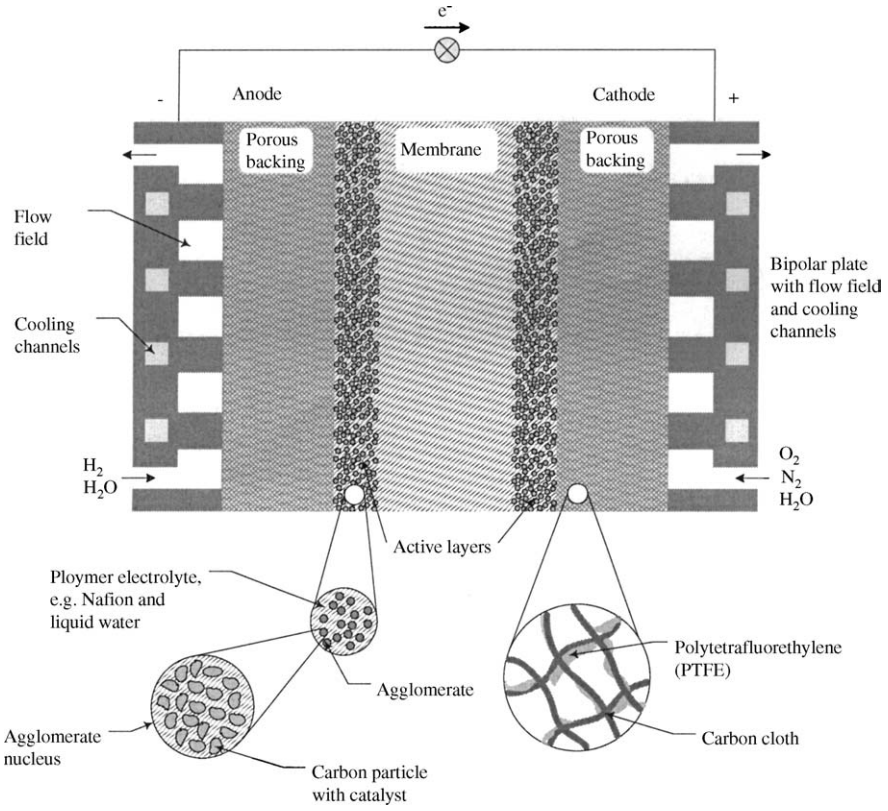

Fig. 1. Schematic of a proton exchange membrane fuel cell.

occurring in a PEM fuel cell. Since a complete fuel cell model would have to address mass, momentum, species and heat transfer in gas and liquid phases in a three-dimensional geometry, as well as the electrokinetics for the ORR and HOR, most models choose to focus on only some of these aspects at a time. The first models to appear were one-dimensional followed by two-dimensional; see [3] for a list of these models. Lately three-dimensional models, based on computational fluid dynamics (CFD), have also begun to appear [4–18]. The main differences between the 3D models are the flow-distributors they study, whether or not multiphase flow is modelled and whether or not a uniform temperature is assumed throughout the cell. Most of these three-dimensional CFD models consider one-phase flow conditions [4–6,8–12,15,17,18], i.e. only take the gas-phase into account in the flow fields and porous backings. While this is a valid approximation, provided the cell temperature is sufficiently high and the partial pressure of the water vapor remains below the saturation value, water vapor tends to condense in the cell and form a liquid phase, especially at higher current densities. Berning et al. [4] and Zhou and Liu [5] developed models to predict the local behaviour of species, temperature and current density in a PEM fuel cell equipped with parallel flow channels; Berning et al. [4] later used theirs for a parameter study of operational, geometric and material properties [6]. An extension by Berning and Djilali [7] to account for the liquid water phase allowed for predictions of the liquid saturation distribution in the cell. Dutta et al. [8] examined the performance of the PEM fuel cell for straight channels with and without the porous backings as well as the water transport through the membrane. The model was later applied by Dutta et al. [9] to elucidate the impact of serpentine flow channels on cell performance. The model by Jen et al. [10] was used to predict cell performance with straight channels. Kumar and Reddy [11] examined the impact of geometrical features such as channel width, depth and shape for serpentine flow fields on cell performance and later also porous metal foams [12], for which they observed a more uniform current density distribution compared to a multi-parallel channel flow field design. Lee et al. [13] extended the model developed by Shimpalee and Dutta [14] to study serpentine flow fields, including experimental validation for the overall water balance. Mazumder and Cole derived both a gas-phase [15] and a multi-phase model [16] to predict cell performance and amount of liquid water. Senn and Poulikakos [17] found that a porous foam led to improved mass transfer and higher cell performance compared to straight and serpentine flow channels. Shimpalee and Dutta [14] developed a model to study various parameters, such as species and temperature distributions for straight channels. The interdigitated flow channel design was compared with straight channels by Um and Wang [18], who found that the interdigitated can sustain a higher mass-transport limited current density than the straight channels. More complex flow field distributors have also been studied, such as the alternative flow field design comprising tree network channels [19]. Based on a ID model, Senn and

Poulikakos [19] found that the tree network structure can sustain higher currents than a parallel flow field design, provided that the fuel cell is designed in a shape that is reminiscent of a double-staircase.

To extend the work on three-dimensional modelling, we have conducted a quantitative comparison of the performance of four common flow-distributors: parallel channels, run in both coflow and counterflow, interdigitated channels and a porous distributor, such as a foam; comparison is carried out with respect both to cell performance and current density uniformity over the catalytic layer. To limit the computational requirements, we assume that the anode side is run at such conditions that it is able to fully sustain any current created at the cathode, i.e. a fully moisturized anode that is run at high stoichiometry. In addition, we assume that sufficient cooling is provided to keep the cathode isothermal, a not unreasonable preliminary assumption in view of the temperature distributions obtained by [4,14], who show that the temperature only varies by a couple of degrees in the cathode. These assumptions enable us then to consider isothermal, three-component, gas-phase, three-dimensional laminar flow in the flow-distributor and adjacent porous backing on the cathode side only.

The mathematical model, consisting of mass, momentum and species transport equations, as well as the geometries of the flow-distributors considered, are introduced in Section 2. We focus also on how a rather detailed agglomerate model for the electrochemical aspects of the active layer, derived by [20], can be simply implemented into the present formulation. Details of the numerical solver used, CFX-4.4 [21], followed by its verification against an asymptotic solution obtained previously [3] are given in Section 3. The results from different flow-distributors are then compared and discussed in Section 4. We finish with conclusions in Section 5.

2. Model description

2.1. Flow-distributor geometry

The electrochemical reactions that occur at the active layers depend on a sufficiently fast transport of reactants to, and products away from, the active sites so as to limit concentration overpotentials. Towards this end, the bipolar plates contain grooved channels, which can take a number of different shapes. Amongst the most common designs today are:

(a) *parallel channels*, with only one pass over the porous backing, run in coflow, as shown in Fig. 2a;
(b) *parallel channels*, with only one pass over the porous backing, run in counterflow, as shown in Fig. 2a;
(c) *interdigitated channels*, where channels are terminated, in order to force the flow into the porous backing, see Fig. 2b;
(d) *a porous material*, such as a foam; here, the entire surface of the porous backing is in contact with the gas flow, see Fig. 2c, in contrast to the channel based flow-distributors, which contain 'dead' zones between the channels. Note that we consider inlets and outlets of the same size as for (a–c), even though a flow field comprising a porous medium can be operated with continuous inlets and outlets. The difference in pressure drop and cell performance between the inlet and outlet configuration chosen here and a continuous counterpart is negligible due to the length to width aspect ratio $L/w_f \gg 1$ (see Table 1);
(e) *serpentine flow channels*, comprising one long channel with many passes over the porous backing;
(f) *a combination of some of the above*, e.g. (a and e), (b and e).

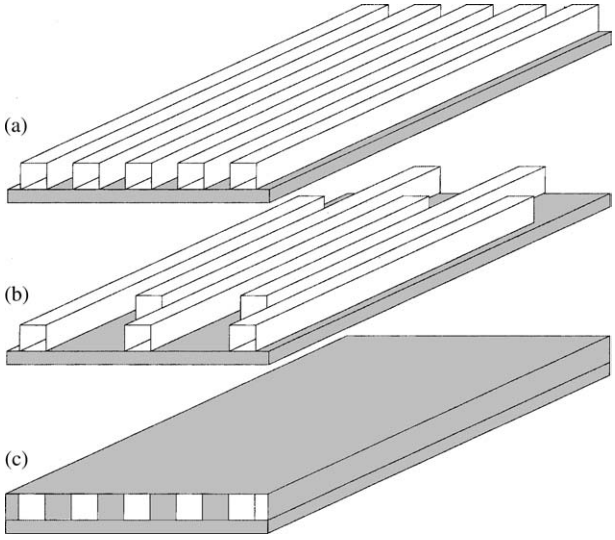

Fig. 2. Schematic of the flow-distributors considered: (a) parallel channels, which can be run in coflow or counterflow; (b) interdigitated flow channels; (c) foam.

We focus here on (a–d).

2.2. Governing equations

2.2.1. Flow channels

In the flow channels, we solve for the momentum and continuity of mass, given by

$$\nabla \cdot (\rho \boldsymbol{v}) = 0, \tag{3}$$

$$\nabla \cdot (\rho \boldsymbol{v} \otimes \boldsymbol{v}) = -\nabla \left(p + \frac{2}{3}\mu \nabla \cdot \boldsymbol{v} \right) + \nabla \cdot (\mu((\nabla \boldsymbol{v}) + (\nabla \boldsymbol{v})^{\mathrm{T}})), \tag{4}$$

where $\boldsymbol{v}$ is the velocity, ρ the density, p the pressure and μ is the dynamic viscosity. The transport equations for the ternary gas mixture, comprising oxygen, water and nitrogen, are

$$\nabla \cdot \left(\rho \boldsymbol{v} \begin{pmatrix} w_{O_2} \\ w_{H_2O} \end{pmatrix} \right) = \nabla \cdot \left(\rho \mathbf{D} \begin{bmatrix} \nabla w_{O_2} \\ \nabla w_{H_2O} \end{bmatrix} \right), \tag{5}$$

Table 1
Base-case parameters

Physical parameters	
γ_b	0.3
γ_f	0.99
$\mathcal{D}_{O_2,H_2O}$	3.98×10^{-5} m^2 s^{-1} at 363 K, 1 atm [20]
$\mathcal{D}_{O_2,N_2}$	2.95×10^{-5} m^2 s^{-1} at 363 K, 1 atm [20]
$\mathcal{D}_{H_2O,N_2}$	4.16×10^{-5} m^2 s^{-1} at 363 K, 1 atm [20]
E_0	1.18 V
M_{O_2}	3.2×10^{-2} kg mol^{-1}
M_{H_2O}	1.8×10^{-2} kg mol^{-1}
M_{N_2}	2.8×10^{-2} kg mol^{-1}
κ_p	10^{-12} m^2
κ_f	10^{-10} m^2
μ	1.812×10^{-5} kg m^{-1} s^{-1}
F	96487 As mol^{-1}
α	0.3
R	8.314 J mol^{-1} K^{-1}
$[M]$	10^{-2} kg mol^{-1}
$[\rho]$	1.0 kg m^{-3}
$p^{vap}_{H_2O}$	4.7×10^{4} N m^{-2} [27]
Operating conditions	
p^{out}	1 atm
L	0.1 m
$\mathfrak{H}^{in}$	30%
T	80 °C (353 K)
h_f	10^{-3} m
h_p	3×10^{-4} m
w_f^1	5×10^{-4} m
w	2×10^{-3} m
Agglomerate model parameters	
r	5×10^{-7} m
α_r	0.78
$\mathcal{A}i_0$	3×10^{3} A m^{-3}
$\mathfrak{D}$	10^{-11} mol m^{-1} s^{-1}
h_a	10^{-5} m
γ_a	0.3
γ_{pol}	0.3
n	4
$c^{ref}_{O_2}$	6.2 mol m^{-3} at $\mathfrak{H}$ = 30%, 1 atm and 353 K

[1] w_f corresponds to the half-width of the flow channels or inlet for the foam in the computational domains due to symmetry conditions.

where w_{O_2} and w_{H_2O} are the mass fractions of oxygen and water and $\mathbf{D}$ is the diffusion tensor.

2.2.2. Porous backing/foam

For porous regions, we have to define superficial and intrinsic properties. Superficial averages are defined as

$$\langle\phi\rangle \equiv \frac{1}{\mathcal{V}}\int_{\mathcal{V}}\phi\,\mathrm{d}\mathcal{V}, \tag{6}$$

and intrinsic, as

$$\langle\phi\rangle^{(g)} \equiv \frac{1}{\mathcal{V}^{(g)}}\int_{\mathcal{V}}\phi\mathcal{V}, \tag{7}$$

where $\mathcal{V}$ is the total volume of the representative elementary volume (REV) and $\mathcal{V}^{(g)}$ is the volume of the gas in the REV. With the porosity, $\gamma = \mathcal{V}^{(g)}/\mathcal{V}$ the two averages are related through

$$\langle\boldsymbol{\phi}\rangle = \gamma\langle\boldsymbol{\phi}\rangle^{(g)}. \tag{8}$$

Conservation of mass and momentum is given, respectively, by

$$\nabla\cdot(\langle\rho\rangle^{(g)}\langle\boldsymbol{v}\rangle) = 0, \tag{9}$$

$$\begin{aligned}\nabla\cdot(\langle\rho\rangle^{(g)}\langle\boldsymbol{v}\rangle\otimes\langle\boldsymbol{v}\rangle) + \mu\mathbf{K}^{-1}\cdot\langle\boldsymbol{v}\rangle \\ = -\nabla\left(\langle p\rangle^{(g)} + \frac{2}{3}\frac{\mu}{\gamma}\nabla\cdot\langle\boldsymbol{v}\rangle\right) \\ +\nabla\cdot\left(\frac{\mu}{\gamma}(\nabla\langle\boldsymbol{v}\rangle + (\nabla\langle\boldsymbol{v}\rangle)^{T})\right),\end{aligned} \tag{10}$$

where $\mathbf{K}$ is the permeability tensor.

The species transport equations are described by

$$\begin{aligned}\nabla\cdot\left(\langle\rho\rangle^{(g)}\langle\boldsymbol{v}\rangle\begin{pmatrix}\langle w_{O_2}\rangle^{(g)}\\ \langle w_{H_2O}\rangle^{(g)}\end{pmatrix}\right) \\ = \nabla\cdot\left(\langle\rho\rangle^{(g)}\gamma\langle\mathbf{D}\rangle^{(g)}\begin{bmatrix}\nabla\langle w_{O_2}\rangle^{(g)}\\ \nabla\langle w_{H_2O}\rangle^{(g)}\end{bmatrix}\right),\end{aligned} \tag{11}$$

where $\langle\mathbf{D}\rangle^{(g)}$ is the total mass diffusion tensor, containing contributions from an intrinsic effective mass diffusion tensor and an intrinsic hydrodynamic dispersion tensor. For a more detailed discussion of these, see [3].

2.3. Boundary conditions

2.3.1. Inlet

At the inlet (see Fig. 3), we prescribe the normal velocity and the gas composition for the channel distributors:

$$\boldsymbol{v}\cdot\mathbf{e}_x = U^{in}, \qquad \boldsymbol{v}\cdot\mathbf{e}_y = \boldsymbol{v}\cdot\mathbf{e}_z = 0, \qquad w_{O_2} = w^{in}_{O_2},$$
$$w_{H_2O} = w^{in}_{H_2O}; \tag{12}$$

in addition, for the counterflow-distributor, we require

$$\boldsymbol{v}\cdot\mathbf{e}_x = -U^{in}, \qquad \boldsymbol{v}\cdot\mathbf{e}_y = \boldsymbol{v}\cdot\mathbf{e}_z = 0, \qquad w_{O_2} = w^{in}_{O_2},$$
$$w_{H_2O} = w^{in}_{H_2O}, \tag{13}$$

for the second channel (see Fig. 3b);

For the foam:

$$\langle\boldsymbol{v}\rangle\cdot\mathbf{e}_x = U^{in}, \qquad \langle\boldsymbol{v}\rangle\cdot\mathbf{e}_y = \langle\boldsymbol{v}\rangle\cdot\mathbf{e}_z = 0,$$
$$\langle w_{O_2}\rangle^{(g)} = w^{in}_{O_2}, \qquad \langle w_{H_2O}\rangle^{(g)} = w^{in}_{H_2O}. \tag{14}$$

2.3.2. Outlet

At the outlet, we specify the pressure and the streamwise gradients of the velocities and species are set to zero, corresponding to fully developed flow conditions. For the channels:

$$p = p^{out}, \tag{15}$$

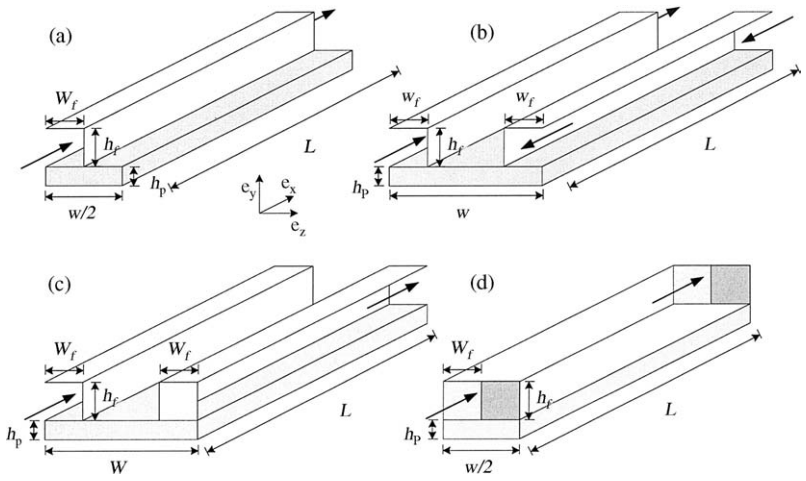

Fig. 3. Schematic of the computational unit cells: (a) parallel channels run in coflow; (b) parallel channels run in counterflow; (c) interdigitated channels; (d) foam.

$$(\mathbf{e}_x \cdot \nabla)(\boldsymbol{v} \cdot \mathbf{e}_y) = 0, \tag{16}$$

$$(\mathbf{e}_x \cdot \nabla)(\boldsymbol{v} \cdot \mathbf{e}_z) = 0, \tag{17}$$

$$\mathbf{e}_x \cdot \nabla w_{O_2} = \mathbf{e}_x \cdot \nabla w_{H_2O} = 0; \tag{18}$$

correspondingly, for the foam:

$$\langle p \rangle^{(g)} = p^{out}, \tag{19}$$

$$(\mathbf{e}_x \cdot \nabla)(\langle \boldsymbol{v} \rangle \cdot \mathbf{e}_y) = 0, \tag{20}$$

$$(\mathbf{e}_x \cdot \nabla)(\langle \boldsymbol{v} \rangle \cdot \mathbf{e}_z) = 0, \tag{21}$$

$$\mathbf{e}_x \cdot \nabla \langle w_{O_2} \rangle^{(g)} = \mathbf{e}_x \cdot \nabla \langle w_{H_2O} \rangle^{(g)} = 0. \tag{22}$$

2.3.3. Walls

At the walls of the channels, we specify no-slip, no normal flow and no componental flux:

$$\boldsymbol{v} = 0, \tag{23}$$

$$\mathbf{n} \cdot \nabla w_{O_2} = \mathbf{n} \cdot \nabla w_{H_2O} = 0, \tag{24}$$

where **n** is the unit normal to a wall. In the porous backing and foam, zero shear stress, no normal flow and no componental flux conditions are applied; these are, respectively

$$(\mathbf{n} \cdot \nabla)(\langle \boldsymbol{v} \rangle \cdot \mathbf{t}) = 0, \tag{25}$$

$$\mathbf{n} \cdot \langle \boldsymbol{v} \rangle = 0, \tag{26}$$

$$\mathbf{n} \cdot \nabla \langle w_{O_2} \rangle^{(g)} = \mathbf{n} \cdot \langle \nabla w_{H_2O} \rangle^{(g)} = 0, \tag{27}$$

where **t** is the unit tangent to a wall.

2.3.4. Symmetry conditions

The flow-distributors considered in this paper are all of periodic character, see Fig. 2, allowing us to reduce the computational domain for each by introducing unit cells, see Fig. 3, with the appropriate symmetry conditions. For the foam and porous backing:

$$(\mathbf{n} \cdot \nabla)(\langle \boldsymbol{v} \rangle \cdot \mathbf{t}) = 0, \tag{28}$$

$$\mathbf{n} \cdot \langle \boldsymbol{v} \rangle = 0, \tag{29}$$

$$\mathbf{n} \cdot \nabla \langle w_{O_2} \rangle^{(g)} = \mathbf{n} \cdot \nabla \langle w_{H_2O} \rangle^{(g)} = 0; \tag{30}$$

correspondingly, for the channels:

$$(\mathbf{n} \cdot \nabla)(\boldsymbol{v} \cdot \mathbf{t}) = 0, \tag{31}$$

$$\mathbf{n} \cdot \boldsymbol{v} = 0, \tag{32}$$

$$\mathbf{n} \cdot \nabla w_{O_2} = \mathbf{n} \cdot \nabla w_{H_2O} = 0. \tag{33}$$

2.3.5. Channel/porous backing interface

At the interface between the porous backing and the flow channels, we couple the pointwise velocities, normal and shear stresses in the plain fluid (flow channels) with their superficial counterparts in the porous medium. The mass fractions and fluxes of oxygen and water are continuous across the interface.

2.3.6. Active region/porous backing interface

The active region in the cathode is sufficiently thin to allow us to treat it as a boundary condition for the porous backing. Using Faraday's Law, the mass fluxes of oxygen and water can be found as

$$\langle \mathbf{n}_{O_2} \rangle \cdot \mathbf{e}_y = -\frac{M_{O_2} \langle \mathbf{i} \rangle \cdot \mathbf{e}_y}{4F}, \tag{34}$$

$$\langle \mathbf{n}_{H_2O} \rangle \cdot \mathbf{e}_y = \frac{(1 + 2\alpha) M_{H_2O} \langle \mathbf{i} \rangle \cdot \mathbf{e}_y}{2F}, \tag{35}$$

where $\langle \mathbf{n}_{O_2} \rangle$ and $\langle \mathbf{n}_{H_2O} \rangle$ are the mass fluxes, α the amount of water dragged through the membrane with each proton, M_i the molecular mass of species i, $\langle \mathbf{i} \rangle$ the superficial current density and F is Faraday's constant. The superficial velocity from the reaction can be derived from the theory of multicomponent mass transfer as

$$\langle \rho \rangle^{(g)} \langle \boldsymbol{v} \rangle \cdot \mathbf{e}_y \frac{\langle \mathbf{i} \rangle \cdot \mathbf{e}_y}{4F} ((2 + 4\alpha) M_{H_2O} - M_{O_2}). \tag{36}$$

2.4. Constitutive relations

Assuming an ideal gas, the gas density can be found from

$$\rho = \frac{pM}{RT}, \tag{37}$$

where $M = (w_{O_2}/M_{O_2} + w_{H_2O}/M_{H_2O} + w_{N_2}/M_{N_2})^{-1}$ is the mean molecular mass, R the universal gas constant and T is the temperature. The mass fraction of nitrogen is given by

$$w_{N_2} = 1 - w_{O_2} - w_{H_2O}. \tag{38}$$

We note here that the molar fractions x_i are related to the mass fractions w_i by

$$x_i = \frac{w_i M}{M_i}. \tag{39}$$

Furthermore, in the most general case, the dynamic viscosity, μ, is also a function of the composition, but for simplicity it is considered constant in this paper. The corresponding constitutive properties in the porous backing and foam are the same, but based on intrinsic values.

An expression for the diffusion tensor [22] can be found from the diffusion coefficients $\tilde{D}_{ij}$ for the molar diffusion flux, relative to a molar-averaged velocity frame, as

$$\tilde{D}_{11} = \frac{\mathcal{D}_{O_2,N_2}(x_{O_2}\mathcal{D}_{H_2O,N_2} + (1 - x_{O_2})\mathcal{D}_{O_2,H_2O})}{S}, \tag{40}$$

$$\tilde{D}_{12} = \frac{x_{O_2}\mathcal{D}_{H_2O,N_2}(\mathcal{D}_{O_2,N_2} - \mathcal{D}_{O_2,H_2O})}{S}, \tag{41}$$

$$\tilde{D}_{21} = \frac{x_{H_2O}\mathcal{D}_{O_2,N_2}(\mathcal{D}_{H_2O,N_2} - \mathcal{D}_{O_2,H_2O})}{S}, \tag{42}$$

$$\tilde{\mathcal{D}}_{22} = \frac{\mathcal{D}_{H_2O,N_2}(x_{H_2O}\mathcal{D}_{O_2,N_2} + (1 - x_{H_2O})\mathcal{D}_{O_2,H_2O})}{S}, \tag{43}$$

$$S = x_{O_2}\mathcal{D}_{H_2O,N_2} + x_{H_2O}\mathcal{D}_{O_2,N_2} + x_{N_2}\mathcal{D}_{O_2,H_2O}, \tag{44}$$

where $\mathcal{D}_{ij}$ are the binary Maxwell–Stefan diffusion coefficients. Since we use the mass diffusion flux relative to the mass-averaged velocity, the following transformation is required:

$$\mathbf{D} = \mathbf{B}\mathbf{W}\mathbf{X}^{-1}\tilde{\mathbf{D}}\mathbf{X}\mathbf{W}^{-1}\mathbf{B}^{-1}, \tag{45}$$

$$\mathbf{B} = \delta_{ij} - w_i\left(1 - \frac{w_n x_j}{x_n w_j}\right), \tag{46}$$

$$\mathbf{X} = x_i\delta_{ij}, \quad i, j = 1, 2, \tag{47}$$

$$\mathbf{W} = w_i\delta_{ij}, \quad i, j = 1, 2, \tag{48}$$

where δ_{ij} is the Kronecker delta. Here, $i, j = 1$ correspond to O_2, $i, j = 2$ correspond to H_2O, and $n = 3$ corresponds to N_2. The binary Maxwell–Stefan diffusion coefficients are corrected for pressure and temperature via [23]:

$$\mathcal{D}_{ij}(T, p) = \frac{p_0}{p}\left(\frac{T}{T_0}\right)^{3/2}\mathcal{D}_{ij}(T_0, p_0). \tag{49}$$

The cross terms in the diffusion tensor $\mathbf{D}$ are around one to two orders of magnitude lower for the operating parameters in this study than the diagonal terms, allowing us to neglect their contributions, whence

$$\mathbf{D} = \begin{bmatrix} D_{11} & 0 \\ 0 & D_{22} \end{bmatrix}. \tag{50}$$

In the porous media, i.e. in the foam and porous backing, we apply a Bruggeman correlation for the superficial effective mass diffusion tensor:

$$\langle\mathbf{D}\rangle = \gamma^{3/2}\mathbf{D}. \tag{51}$$

The permeabilities of the porous backing and foam are taken to be isotropic

$$\mathbf{K} = \kappa\delta_{ij}, \tag{52}$$

where κ is the permeability.

2.5. Electrokinetics and the active layer

An expression is still required for the current density $\langle\mathbf{i}\rangle\cdot\mathbf{e}_y$ given in equation (36). A novel feature of this paper is to implement an expression from an agglomerate model derived by Jaouen et al. [20], and subsequently validated experimentally [24]. Although [20] considers an active layer of finite thickness, it is possible to demonstrate that, for our purposes, the active layer need not be resolved explicitly, but rather can be treated implicitly as a boundary condition. Some further details are as follows.

The volumetric current density $\langle i_v\rangle$, given by [20], is approximated as

$$\langle i_v\rangle = Ai_0(1 - \gamma_{pol})(1 - \gamma_a)\exp\left(-\frac{\alpha_r F}{RT}\eta\right)\mathfrak{F}\frac{\langle c_{O_2}\rangle^{(g)}}{c_{O_2}^{ref}}, \tag{53}$$

where $\mathcal{A}i_0$ is the volumetric exchange current density in the agglomerates, γ_{pol} the volume fraction of the polymer electrolyte in the agglomerate nucleus, $\langle c_{O_2}\rangle^{(g)} = \langle w_{O_2}\rangle^{(g)}\langle\rho\rangle^{(g)}/M_{O_2}$ the molar concentration of oxygen, α_r the cathodic transfer coefficient for the ORR, η the overpotential at the cathode (defined negative) and γ_a is the volume fraction of pores in the active layer. $\mathfrak{F}$ is the nucleus effectiveness factor, defined as

$$\mathfrak{F} = \frac{3}{\Upsilon r}\left(\frac{1}{\tanh(\Upsilon r)} - \frac{1}{\Upsilon r}\right), \tag{54}$$

with Υ given by

$$\Upsilon = \sqrt{\frac{Ai_0(1 - \gamma_{pol})\exp(-\frac{\alpha_r F}{RT}\eta)}{nF\mathfrak{D}}}, \tag{55}$$

where $\mathfrak{D}$ is an effective oxygen permeability in the agglomerates, n the number of electrons consumed in the ORR per oxygen molecule and r is the radius of the agglomerate nucleus.

This agglomerate model was validated by [24] for a small PEM fuel cell with an area of 2 cm^2 at conditions well above the stoichiometric flow rate, allowing the cell there to be modelled one-dimensionally, since concentration gradients in the streamwise direction in the cathode could be neglected. In this paper, however, the aim is to capture and study two- and three-dimensional effects. The one-dimensional agglomerate model can be used for this purpose by noting that the geometry of the active layer studied is slender, i.e. its thickness, h_a, is much smaller than its width (w) and breadth (L), implying that only gradients in the normal direction in the active layer will contribute to mass transfer; consequently, this allows us to treat the active layer locally as one-dimensional. Although we omit the details here, it is possible to show by scale analysis that we will not have any gradients of oxygen in the normal direction in the active layer, since the magnitude of the diffusion coefficient in the agglomerates is $O(10^{-13})\,m^2\,s^{-1}$, as compared to $O(10^{-5})\,m^2\,s^{-1}$ in the pores. The additional approximation of reducing the active layer to a boundary condition corresponds to an infinite effective proton conductivity in the active layer. The total current density is then given locally by $\langle \mathbf{i} \rangle \cdot \mathbf{e}_y = \langle i \rangle = \langle i_v \rangle h_a$.

Jaouen et al. [20] discerned four different regimes, where the Tafel slope doubles or even quadruples, and subsequently supplied the experimental validation to support these [24]. In regime 1, the active layer is controlled by Tafel kinetics and is first order in the oxygen concentration. Regime 2 displays a doubling of the Tafel slope, due to the active layer being governed by Tafel kinetics and oxygen diffusion in the agglomerates, but still remains first-order in the oxygen concentration. A doubling of the Tafel slope is observed in the third regime, where the active layer is controlled by the Tafel kinetics, in addition to proton migration. The oxygen dependence here is half-order. The final regime, the fourth, shows a quadrupling of the Tafel slope, and is attributable to an active layer controlled by Tafel kinetics, proton migration and oxygen diffusion in the agglomerates. The oxygen dependence is half-order, as in regime 3.

By assuming that we have no resistance to proton migration, we limit the validity of the expression to regimes 1 and 2, i.e. to an active layer controlled by Tafel kinetics at low overpotentials, and at higher overpotentials by Tafel kinetics coupled with oxygen diffusion resistance in the agglomerates. We are thus able to capture the doubling of the Tafel slope due to mass transfer limitations in the agglomerates, although the doubling due to proton migration resistance and a quadrupling of the slope are not modelled.

Finally, we note that of more use, as regards judging fuel cell performance, than the overpotential, η, is the cell voltage, E_{cell}, where

$$\eta = E_{cell} - E_0, \tag{56}$$

and E_0 is the equilibrium potential.

3. Numerics and verification

A commercial computational fluid dynamics code, CFX-4.4, based on finite volumes, was used to implement the model outlined above. As can be seen in Fig. 2, all of the flow-distributors are periodic in the spanwise direction. Hence, a representative computational unit cell, with symmetry boundary conditions on both sides in the spanwise coordinate, can be introduced. The unit cells for the distributors are chosen so that the area of the active layer and the contact area between the channels and porous backing are the same for all, with the exception of the foam, which covers the entire porous backing as depicted in Fig. 3.

Using a structured mesh, each flow-distributor with porous backing was resolved as follows:

(a) *Parallel channels run in coflow*: The channel contained 10^4 computational cells and the porous backing 2×10^4 cells, giving a total of 3×10^4 cells. Mesh independence was assured by comparing with a mesh comprising 1.2×10^5 cells and the difference was found to be ~1% for the average current density.

(b) *Parallel channels run in counterflow*: The two channels with 10^4 cells each and the porous backing with 4×10^4 cells, giving a total of 6×10^4 cells. Mesh independence was assured by comparing with a mesh comprising 2×10^5 cells and the difference was found to be ~1% for the average current density.

(c) *Interdigitated channels*: The two channels with 10^4 cells each and the porous backing with 4×10^4, giving a total of 6×10^4 cells. Mesh independence was assured by comparing with a mesh comprising 2×10^5 cells and the difference was found to be ~4% for the average current density. At higher currents, i.e. $\langle i \rangle > 4\,A\,cm^{-2}$, more than 6×10^4 cells were necessary to resolve the flow in the porous backing. We did not pursue these higher current densities, however.

(d) *Foam*: The foam and porous backing, each with 2×10^4 cells, giving a total of 4×10^4 cells. Mesh independence was assured by comparing with a mesh comprising 1.6×10^5 cells and the difference was found to be ~1% for the average current density.

The computations, carried out on a 500 MHz Compaq Alphaserver with 3 GB RAM, required about 1–2 h for lower current densities and about 12 h for higher.

The numerical code was verified via asymptotic solutions [3], who showed that for a slender two-dimensional geometry, consisting of a flow channel adjacent to the porous backing, closed form solutions could be found for $\Delta = 1/(Re\sigma^2) \gg 1$, where Re ($=\rho U^{in} L/\mu$) is the Reynolds number, and $\sigma = h_f/L$, with h_f and L as the height and length of the flow-distributor. The geometry is depicted in Fig. 4 in dimensional form. For the asymptotic analysis, the governing equations are scaled so that $X = x/L$, $Y = y/h_f$. For a current density which can be written non-dimensionally on the form $I = \langle x_{O_2} \rangle^{(g)}$, where

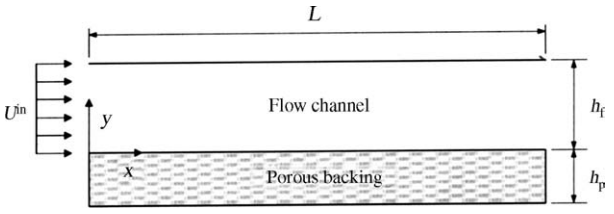

Fig. 4. The two-dimensional cathode with a flow-distributor above the porous backing.

$I = \langle i \rangle / [i]$ and $[i]$ is the current density scale, the leading order solution was found to be given by

$$A \log\left(\frac{\zeta_{O_2}(X)(\Phi\zeta_{O_2}(0)+1)}{\zeta_{O_2}(0)(\Phi\zeta_{O_2}(X)+1)}\right) - (A\Phi - B)\left(\frac{\zeta_{O_2}(X)-\zeta_{O_2}(0)}{(\Phi\zeta_{O_2}(X)+1)(\Phi\zeta_{O_2}(0)+1)}\right) = \frac{\Omega X}{4\rho_0(0)(\Phi\zeta_{O_2}(0)+1)},$$

where

$$\mathcal{A} = \frac{1}{\mathcal{M}_{N_2}}\left((\mathcal{M}_{H_2O} - \mathcal{M}_{N_2}) \times \left(\frac{(2+4\alpha)\zeta_{O_2}(0)+\zeta_{H_2O}(0)}{\Phi\zeta_{O_2}(0)+1}\right) - 1\right), \quad (57)$$

$$\mathcal{B} = \frac{1}{\mathcal{M}_{N_2}}\left((\mathcal{M}_{O_2} - \mathcal{M}_{N_2}) + (\mathcal{M}_{H_2O} - \mathcal{M}_{N_2}) \times \left(\frac{\Phi\zeta_{H_2O}(0) - (2+4\alpha)}{\Phi\zeta_{O_2}(0)+1}\right)\right), \quad (58)$$

and

$$\zeta_{O_2} = \frac{x_{O_2}}{\mathcal{M}}, \quad (59)$$

$$\zeta_{H_2O} = \frac{(1+\Phi\zeta_{O_2}(X))\zeta_{H_2O}(0) + (2+4\alpha)(\zeta_{O_2}(0) - \zeta_{O_2}(X))}{\Phi\zeta_{O_2}(0)+1}, \quad (60)$$

with, $\mathcal{M}_i = M_i/[M]$, $\mathcal{M} = M/[M]$, where $[M]$ is a molecular weight scale, $\Omega = \frac{[i][M]}{[\rho]U^{in}F\sigma}$ and $\Phi = (2+4\alpha)\mathcal{M}_{H_2O} - \mathcal{M}_{O_2}$. For the agglomerate model applied here, we obtain the current density scale:

$$[i] = \mathcal{A}i_0(1-\gamma_{pol})(1-\gamma_a)\exp\left(-\frac{\alpha_r F}{RT}\eta\right)\mathfrak{F}\frac{h_a[\rho]}{c_{O_2}^{ref}[M]}, \quad (61)$$

whence $I \equiv \langle x_{O_2} \rangle^{(g)}$ as required for the solution above.

Comparison, shown in Fig. 5, was carried out in terms of mass fraction profiles along the cathode. All parameters from the base case were used, see Table 1, but with $\Delta = 960$, $\sigma = 10^{-3}$ and $\Omega = 28.2$. The number of cells used for this 2D calculation in CFX-4.4 were 2000. The mass fractions obtained with CFX-4.4 agree well with the ones obtained analytically.

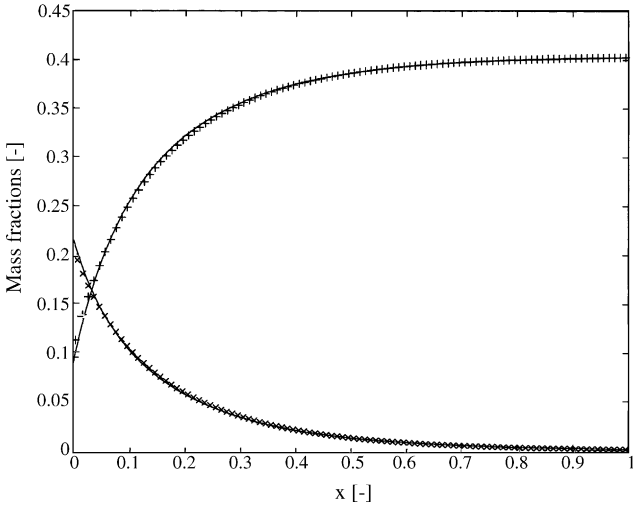

Fig. 5. Verification of the CFX-4.4 code. (—) Corresponds to analytical solutions and markers are for the CFX-4.4 solutions; (+) water mass fraction; (×) oxygen mass fraction.

4. Results and discussion

For each flow-distributor, simulations were carried out for six different cell potentials, E_{cell}. However, rather than specifying the inlet velocity, U^{in}, we specify instead, as tends to be the practice in experimental work with fuel cells, the stoichiometry, ξ, which is defined by

$$\xi = \frac{\int_{A^{in}} n_{O_2}^{in}\,dA}{\int_{A^{cat}}\left\langle n_{O_2}^{cat}\right\rangle dA} = \frac{\rho U^{in} w_{O_2}^{in} A^{in}}{M_{O_2}/4F\int_{A^{cat}}\langle i\rangle\,dA'}, \quad (62)$$

where $n_{O_2}^{in}$ and $\left\langle n_{O_2}^{cat}\right\rangle$ are the mass fluxes of oxygen into the cathode and of the oxygen being consumed at the active layer, respectively, and A^{cat} and A^{in} are the total areas of the active layer and the inlet. This formulation implies that the inlet velocity is iterated for, its value depending on the current density obtained at the catalytic layer on the previous iteration. We also specify the relative humidity at the inlet, $\mathfrak{H}^{in}$, given by

$$\mathfrak{H}^{in} = \frac{x_{H_2O}^{in} p^{in}}{p_{H_2O}^{vap}}, \quad (63)$$

where $p_{H_2O}^{vap}$ is the vapor pressure of water; furthermore, since $x_{O_2}/x_{N_2} = 21/79$ and $x_{O_2} + x_{H_2O} + x_{N_2} = 1$, we have the inlet compositions for a given relative humidity as

$$x_{H_2O}^{in} = \mathfrak{H}^{in}\frac{p_{H_2O}^{vap}}{p^{in}}, \qquad x_{O_2}^{in} = \frac{1 - x_{H_2O}^{in}}{1 + 79/21}. \quad (64)$$

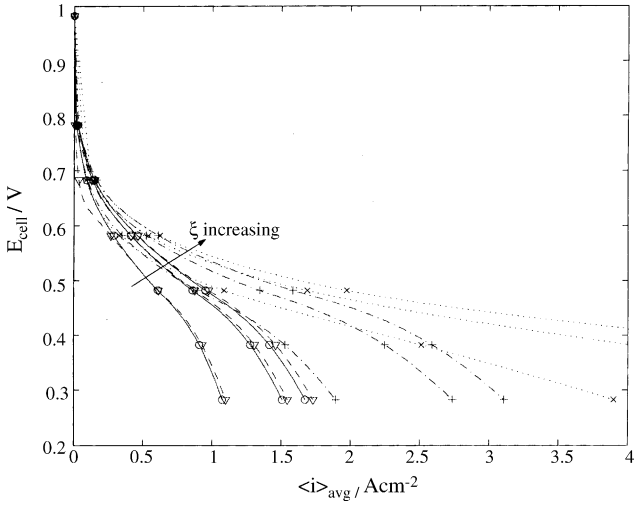

Fig. 6. Polarization curves for the different flow-distributors at stoichiometry $\xi = 1.5, 3, 5$: coflow channels (◯), counterflow channels (▽), interdigitated channels (×), foam (+).

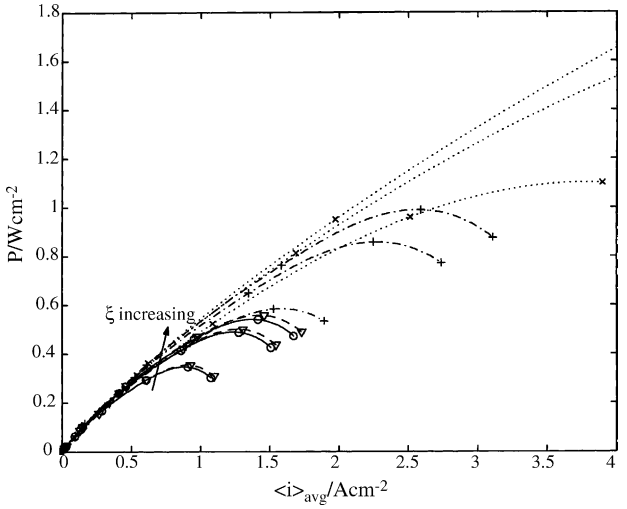

Fig. 7. Power density, P, for the different flow-distributors at stoichiometry $\xi = 1.5, 3, 5$: coflow channels (◯), counterflow channels (▽), interdigitated channels (×), foam (+).

Consequently, $x^{\text{in}}_{\text{H}_2\text{O}}$ and $x^{\text{in}}_{\text{O}_2}$ must also be updated at every iteration.

Earlier work [25,26], albeit in 2D models, suggests that the interdigitated design should be capable of yielding higher current densities than either one of the straight channel designs considered here. Also, we expect that either the foam or the interdigitated channels give rise to the highest average current densities, since the interdigitated design forces the flow into the porous backing, whereas the foam covers the whole surface of the porous backing. The foam has already been shown to be more efficient in terms of higher current densities and power density than serpentine flow channels [17]. Parallel channels run in counterflow might be expected to perform better than channels in coflow, as the former allows for alternating inlets and outlets, thus providing for an increased mass transfer in the spanwise direction. This is indeed the case, as can be seen in Fig. 6, where the polarization curves for the stoichiometries 1.5, 3 and 5 are shown. The interdigitated design allows for average current densities of 4 A cm^{-2} for cell potentials between 0.3 and 0.4 V, depending on stoichiometry. Current densities ranging from 2 to 3.2 A cm^{-2} are obtainable with the foam. The counterflow gives somewhat higher current densities than the coflow design, especially for the higher stoichiometry.

Fig. 7 depicts the power density for the flow-distributors. In the lower ranges of current density, 0–0.4 A cm^{-2}, the power density is independent of the type of distributor used. As the current density is increased, differences between the flow designs become readily apparent, with the interdigitated sustaining the highest power densities, followed by the foam. The counterflow channels perform marginally better than the coflow channels.

The performance of a fuel cell is judged not only on the magnitude of current density that can be generated, but also on the uniformity of the current distribution at the active layer, since uniformity is linked to catalyst utilization and degradation. As a measure of the uniformity, we compare the standard deviation of the current density for each flow design, σ_{std}, defined by

$$\sigma_{\text{std}} = \left(\frac{1}{A^{\text{cat}}} \int_{A^{\text{cat}}} (\langle i \rangle - \langle i \rangle_{\text{avg}})^2 \, \mathrm{d}A' \right)^{1/2},$$

where

$$\langle i \rangle_{\text{avg}} = \frac{1}{A^{\text{cat}}} \int_{A^{\text{cat}}} \langle i \rangle \, \mathrm{d}A', \tag{65}$$

as illustrated in Fig. 8. For all flow-distributors, the distribution becomes more uniform as the stoichiometry is increased. At a stoichiometry of 1, all the oxygen that enters the cathode would be consumed; by increasing the stoichiometry, the flow

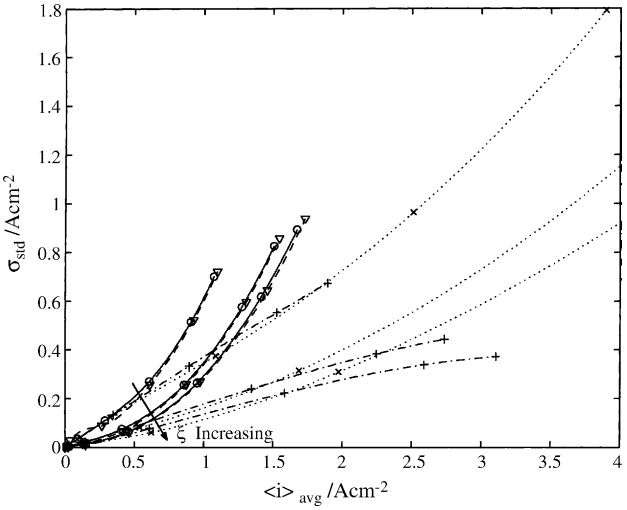

Fig. 8. Standard deviation of the current density, σ_{std}, for the different flow-distributors at stoichiometry $\xi = 1.5, 3, 5$: coflow channels (◯), counterflow channels (▽), interdigitated channels (×), foam (+).

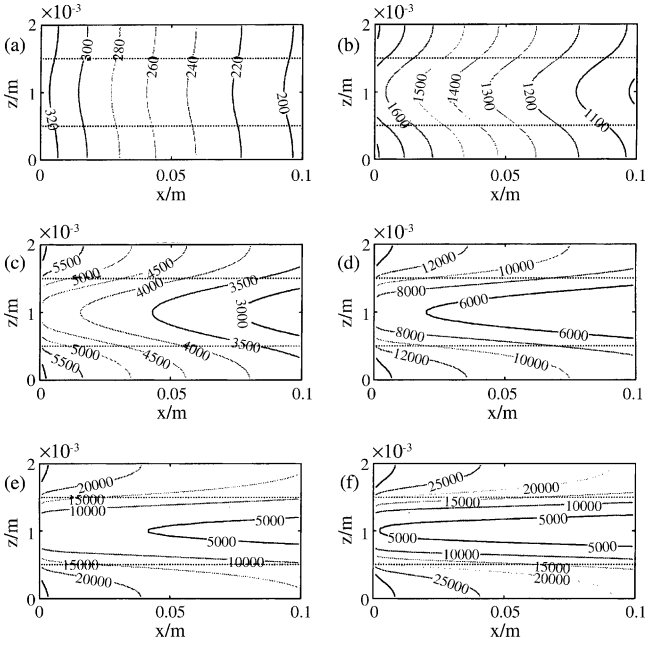

Fig. 9. The local current density distribution for the coflow-distributor at the active layer for different potentials at stoichiometry $\xi = 3$: (a) $E_{cell} = 0.782$ V; (b) $E_{cell} = 0.682$ V; (c) $E_{cell} = 0.582$ V; (d) $E_{cell} = 0.482$ V; (e) $E_{cell} = 0.382$ V; (f) $E_{cell} = 0.282$ V.

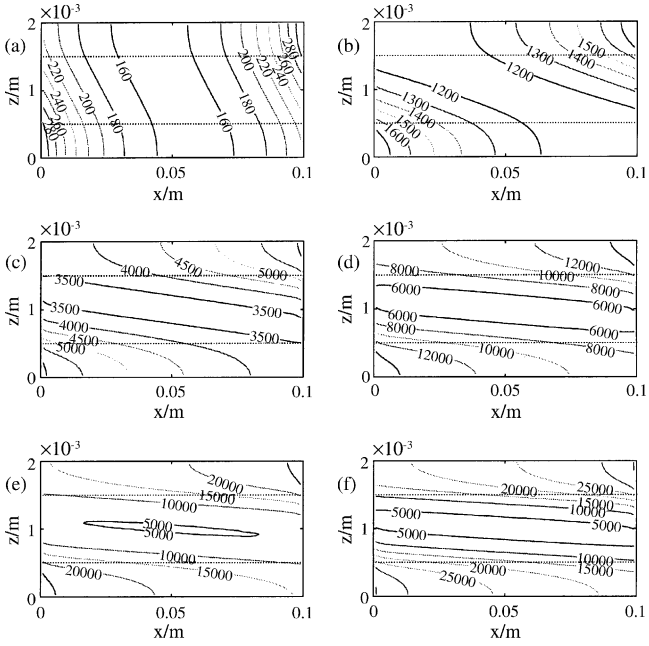

Fig. 10. The local current density distribution for the counterflow-distributor at the active layer for different potentials at stoichiometry $\xi = 3$: (a) $E_{cell} = 0.782$ V; (b) $E_{cell} = 0.682$ V; (c) $E_{cell} = 0.582$ V; (d) $E_{cell} = 0.482$ V; (e) $E_{cell} = 0.382$ V; (f) $E_{cell} = 0.282$ V.

becomes less depleted of oxygen, and is hence able to sustain higher current and a more uniform distribution. The parallel channels, run in co- and counterflow, exhibit the highest deviations at current densities above $\sim$0.4 A cm^{-2}, with the coflow being the less uniform of the two. At current densities below 1.5–2 A cm^{-2}, depending on stoichiometry, greatest uniformity is obtained for the interdigitated design, but the extent of the non-uniformity increases with the current; ultimately, the foam design gives the greatest uniformity. These findings are also reflected in Figs. 9–12, where the local current density for different cell potentials is given. All distributors exhibit a more non-uniform current density as the overpotential is increased, i.e. as the cell voltage decreases. For coflow (see Fig. 9), the areas under the flow channels can sustain local higher current densities than those under the "rib" of the bipolar plate, where mass transfer becomes increasingly limiting with increasing overpotential. The cathode operated in counterflow behaves similarly (Fig. 10), but delivers a somewhat higher overall performance, as the counterflow arrangement allows for exiting air with a lower oxygen concentration in one channel to be balanced by incoming fresh air in the two adjacent channels. For the foam (Fig. 11), the local current density is a function of the streamwise coordinate only, although there are minor inlet and exit effects, which become somewhat more pronounced at higher current densities. This simplification is attributable to the inherent characteristic of the foam to cover the surface of the porous backing, in contrast to grooved channels in a bipolar plate comprising alternating regions of channels and ribs. Finally, the interdigitated arrangement (Fig. 12) displays an increasingly spanwise behaviour for the local current density at higher overpotentials. The overall flow increases for a given stoichiometry at higher current densities, leading to increased forced convective flow in the porous backing, whence the local current density becomes more even in the spanwise direction.

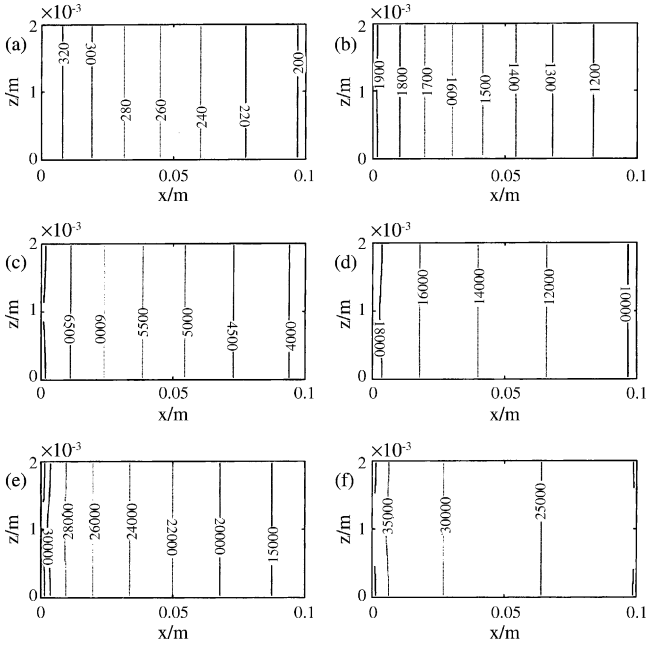

Fig. 11. The local current density distribution for the foam distributor at the active layer for different potentials at stoichiometry $\xi = 3$: (a) $E_{cell} = 0.782$ V; (b) $E_{cell} = 0.682$ V; (c) $E_{cell} = 0.582$ V; (d) $E_{cell} = 0.482$ V; (e) $E_{cell} = 0.382$ V; (f) $E_{cell} = 0.282$ V.

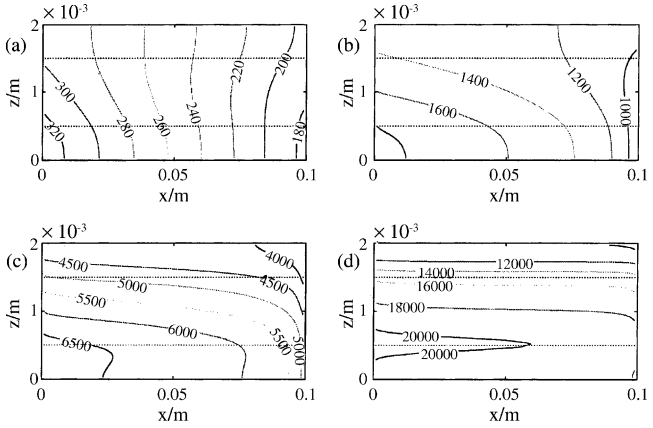

Fig. 12. The local current density distribution for the interdigitated flow-distributor at the active layer for different potentials at stoichiometry $\xi = 3$: (a) $E_{cell} = 0.782$ V; (b) $E_{cell} = 0.682$ V; (c) $E_{cell} = 0.582$ V; (d) $E_{cell} = 0.482$ V.

Keeping the pressure drop, Δp ($= p^{in} - p^{out}$), at a minimum is of interest in terms of reducing operating costs for the fuel cell, whence a good flow-distributor should be able to sustain high even current densities, whilst keeping the pressure drop to a minimum. The foam, as shown in Fig. 13, requires the highest pressure drop to drive the flow; this can be attributed to the rather low permeability chosen for the foam in this study. An increase in permeability to 10^{-8} m^2 would lead to a reduction of the pressure drop by approximately two orders of magnitude, as can be estimated from Darcy's law. The pressure drop for the interdigitated distributor is higher than for the coflow and counterflow, which is to be expected since the flow is being forcibly driven through the porous backing, in this study with a permeability of 10^{-12} m^2. The lowest pressure drops are obtained with the parallel channels, with no discernible difference in the magnitude of the pressure drop between the two.

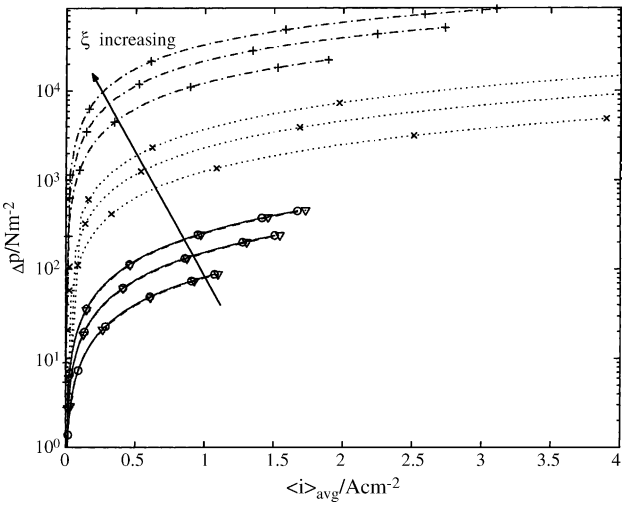

Fig. 13. Pressure drop, Δp, for the different flow-distributors at stoichiometry $\xi = 1.5$, 3, 5: coflow channels (◯), counterflow channels (▽), interdigitated channels (×), foam (+).

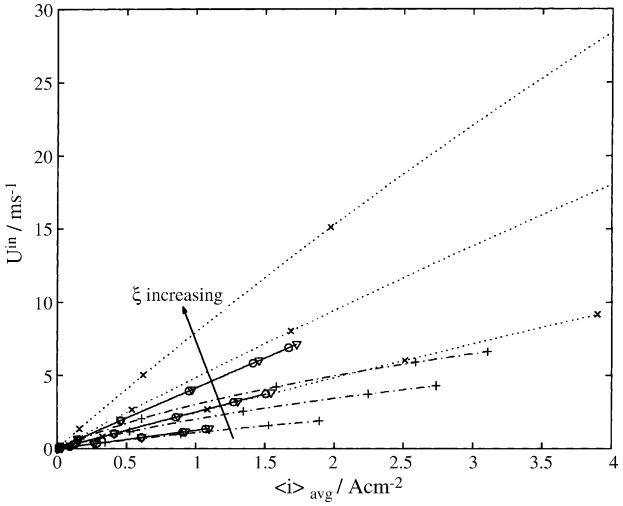

Fig. 14. Obtained inlet velocity, U^{in}, for the different flow-distributors at stoichiometry $\xi = 1.5$, 3, 5: coflow channels (◯), counterflow channels (▽), interdigitated channels (×), foam (+).

Since we do not specify the inlet velocity, but rather iterate on it to obtain a given stoichiometry for a specified cell potential, it is of interest to see how the inlet velocity changes with current density and stoichiometry; this is shown in Fig. 14. The inlet velocity is almost proportional to the average current density, and only starts to deviate from linear when the density at the inlet changes due to the pressure drop obtained. The reason why the inlet velocities for the interdigitated channels are higher is because the inlet area is half as large as for the other flow-distributors.

5. Conclusions

A study of different flow-distributors, based on a gas-phase model for mass, momentum and species transport in the cathode of a PEM fuel cell, has been considered. Special attention was given to the treatment of the active layer, for which an agglomerate model developed previously [20] was used. The numerical code used was verified with an analytical solution, also developed previously [3]. The novel features of this study are: (1) a direct quantitative comparison of the performance of different flow-distributors and (2) the use of a new agglomerate model which agrees well with experimental observations for a small fuel cell [24]. The complete validation of the gas-phase model considered here would require more detailed information about the local current density distribution; in future, this will be obtainable via experiments with a segmented cell.

The aim of the study was to compare the performance of different flow-distributors for a given cell at a given potential, in terms of four different quantities: the obtained average current density, power density, standard deviation of the current density distribution and pressure drop. The results show that the interdigitated flow-distributor can sustain the high-

est current densities, but at a higher pressure drop than the counterflow and coflow channels. Furthermore, to function properly, the interdigitated channels would have to be in contact with the porous backing in such a way that channeling effects are kept at a minimum; given the high velocities required, even the slightest gap might lead to most of the flow going through the gap and not through the porous backing, with a resulting loss of power density. A foam distributor is able to give the lowest standard deviation for the current at high current densities, but care should be taken as to its permeability to avoid an unreasonably high pressure drop.

The present work was limited to gas-phase flow and isothermal conditions. Future work will seek to carry out a comparative study that incorporates both the possible production of liquid water at the catalytic layer and non-isothermal effects.

Acknowledgements

Financial support from the Swedish Foundation for Strategic Environmental Research, MISTRA and from the Swedish National Energy Administration is gratefully acknowledged. The work was done within the framework of the Jungner Center.

References

[1] C.K. Dyer, Fuel cells for portable applications, J. Power Sources, Proceedings of the Seventh Grove Fuel Cell Symposium, 106 (2002) 31–34.
[2] J.M. Moore, J.B. Lakeman, G.O. Mepsted, Development of a PEM fuel cell powered portable field generator for the dismounted soldier, J. Power Sources, Proceedings of the Seventh Grove Fuel Cell Symposium, 106 (2002) 16–20.
[3] M. Vynnycky, E. Birgersson, Analysis of a model for multicomponent mass transfer in the cathode of a polymer electrolyte fuel cell, SIAM J. Appl. Maths 63 (2003) 1392–1423.
[4] T. Berning, D.M. Lu, N. Djilali, Three-dimensional computational analysis of transport phenomena in a PEM fuel cell, J. Power Sources 106 (2002) 284–294.
[5] T. Zhou, H. Liu, A general three-dimensional model for proton exchange membrane fuel cells, Int. J. Transport Phenomena 3 (2001) 177–198.
[6] T. Berning, N. Djilali, Three-dimensional computational analysis of transport phenomena in a PEM fuel cell—a parametric study, J. Power Sources 124 (2003) 440–452.
[7] T. Berning, N. Djilali, A 3D, multiphase, multicomponent model of the cathode and anode of a PEM fuel cell, J. Electrochem. Soc. 150 (12) (2003) A1589–A1598.
[8] S. Dutta, S. Shimpalee, J.W. van Zee, Three-dimensional numerical simulation of straight channel PEM fuel cells, J. Appl. Electrochem. 30 (2000) 135–146.
[9] S. Dutta, S. Shimpalee, J.W. van Zee, Numerical prediction of mass-exchange between cathode and anode channels in a PEM fuel cell, Int. J. Heat Mass Transfer 44 (2001) 2029–2042.
[10] T.-C. Jen, T. Tan, S.-H. Chan, Chemical reacting transport phenomena in a PEM fuel cell, Int. J. Heat Mass Transfer 46 (2003) 4157–4168.
[11] A. Kumar, R.G. Reddy, Effect of channel dimensions and shape in the flow-field distributor on the performance of polymer electrolyte membrane fuel cells, J. Power Sources 113 (2003) 11–18.
[12] A. Kumar, R.G. Reddy, Modeling of polymer electrolyte membrane fuel cell with metal foam in the flow-field of the bipolar/end plates, J. Power Sources 114 (2003) 54–62.
[13] W.-K. Lee, S. Shimpalee, J.W. van Zee, Verifying predictions of water and current distributions in a serpentine flow field polymer electrolyte membrane fuel cell, J. Electrochem. Soc. 150 (3) (2003) A341–A348.
[14] S. Shimpalee, S. Dutta, Numerical prediction of temperature distribution in PEM fuel cells, Num. Heat Transfer Part A 38 (2000) 111–128.
[15] S. Mazumder, J.V. Cole, Rigorous 3-D mathematical modeling of PEM fuel cells. I. Model predictions without liquid water transport, J. Electrochem. Soc 150 (2003) A1503–A1509.
[16] S. Mazumder, J.V. Cole, Rigorous 3-D mathematical modeling of PEM fuel cells. II. Model predictions with liquid water transport, J. Electrochem. Soc. 150 (2003) A1510–A1517.
[17] S.M. Senn, D. Poulikakos, Polymer electrolyte fuel cells with porous materials as fluid distributor and comparisons with traditional channeled systems, J. Heat Transfer Trans. ASME 126 (2004) 410–418.
[18] S. Um, C.Y. Wang, Three-dimensional analysis of transport and electrochemical reactions in polymer electrolyte fuel cells, J. Power Sources 125 (2004) 40–51.
[19] S.M. Senn, D. Poulikakos, Tree network channels as fluid distributors constructing doublestair-case polymer electrolyte fuel cells, J. Appl. Phys. 96 (1) (2004) 842–852.
[20] F. Jaouen, G. Lindbergh, G. Sundholm, Investigation of mass-transport limitations in the solid polymer fuel cell cathode. I. Mathematical model, J. Electrochem. Soc. 149 (2002) A437–A447.
[21] CFX-4.4, http://www.cfx.aeat.com.
[22] R. Taylor, R. Krishna, Multicomponent Mass Transfer, John Wiley and Sons, USA, 1993.
[23] J.R. Welty, C.E. Wicks, R.E. Wilson, Fundamentals of Momentum, Heat and Mass Transfer, third ed., John Wiley and Sons, USA, 1984.
[24] J. Ihonen, F. Jaouen, G. Lindbergh, A. Lundblad, G. Sundholm, Investigation of mass-transport limitations in the solid polymer fuel cell cathode. II. Experimental, J. Electrochem. Soc. 149 (2002) A448–A454.
[25] J.S. Yi, T. Van Nguyen, Multicomponent transport in porous electrodes of proton exchange membrane fuel cells using the interdigitated gas distributors, J. Electrochem. Soc. 146 (1999) 38–45.
[26] A. Kazim, H.T. Liu, P. Forges, Modelling of performance of PEM fuel cells with conventional and interdigitated flow fields, J. Appl. Electrochem. 29 (1999) 1409–1416.
[27] M.J. Moran, H.N. Shapiro, Fundamentals of Engineering Thermodynamics, second ed., John Wiley and Sons, USA, 1993.